Prototype Readout Electronics System for a LET Spectrometer in Space Radiation

Wenrui Sun, Yuxuan Chen, Zhe Cao, Li Wang, Yifan Qiao, Chunjuan Li, Li Xia, Yunju Li

***Abstract*—Space radiation has been widely investigated by researches around the world. Linear energy transfer (LET) is widely used for quantitatively assessing the effects of space radiation. Space radiation is characterized by a heterogeneous composition of particle types, a broad energy spectrum, and temporal variability, making it difficult to achieve high-precision and large dynamic range real-time LET detection. In this paper，a prototype readout electronics system is proposed. The prototype system is designed for a LET spectrometer using a novel dynamic range extension method, achieving a large dynamic range and high measurement precision in real-time detection. This prototype system is developed for silicon telescopes composed of double-sided silicon strip detectors (DSSDs) of 3 layers. It contains 3 front-end electronics (FEE) modules, and 1 data acquisition module (DAM). Electrical tests show that the charge dynamic range is up to about 700 fC while the equivalent charge noise (ENC) of the prototype in high gain mode is about 0.11 fC. The extended dynamic range is about 6000. To validate the LET measurement methodology, a neutron radiation field test was conducted. GEANT4-based simulations were performed to verify the correctness of the experimental results. The experimental results show good agreement with simulations.**

***Index Terms*—Linear energy transfer (LET), double-sided silicon strip detector (DSSD), readout electronics, dynamic range extension method.**

I. Introduction

SPACE radiation has been widely investigated by researchers around the world. Space radiation consists of galactic cosmic rays (GCRs), solar particle events (SPEs), and particles trapped in earth's radiation belts (ERBs). It is characterized by a heterogeneous composition of particle types, a broad energy spectrum, and temporal variability and anisotropic incidence directions [1, 2]. It is challenging to detect precisely and comprehensively

Linear energy transfer (LET) is widely employed in space radiation researches, for instance, to assessment of radiation-induced damage to human body and semiconductor devices [3]. It quantitatively assesses the effects of space radiation. It provides a quantitative measure of the effects of space radiation. The definition of LET is given by (1), where ΔE denotes the total energy deposited and Δl represents the total path length traversed. LET thus corresponds to the energy deposited per unit path of specific material [4]. In practice, LET values are typically converted to the equivalent LET in an infinite volume of water.

$$LET = \Delta E/\Delta l \quad (1)$$

It is impractical to monitor all components of space radiation with a single instrument. A practical compromise is to monitor the most abundant components. As shown in Fig. 1, relativistic particles with atomic numbers Z ranging from 1 to 26 are the dominant constituents of GCRs. Protons and electrons are the primary components of SPEs and ERBs. Therefore, relativistic particles with $1 \leqslant Z \leqslant 26$ can serve as a baseline for this study. According to the Bethe–Bloch formula [5], the energy deposition is proportional to Z^2, yielding a relative dynamic range of approximately 680. Considering that the average LET for minimum ionizing particles (MIPs) is 0.2 keV/μm in water, the corresponding LET range extends from 0.2 to 136 keV/μm (H_2O). Furthermore, the flux in the LET spectrum obtained by the HEZTRN model [6] for a spacecraft exhibits a significant decrease for LET values exceeding 136 keV/μm in water.

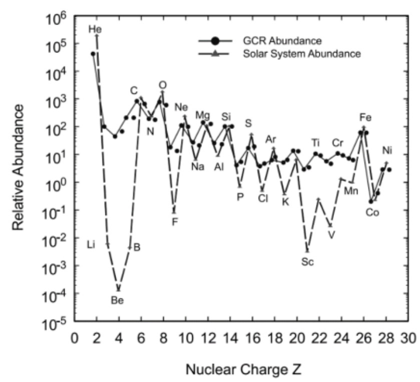

Fig. 1. Relative abundance of GCR particles [7].

High energy and position resolution, a large dynamic range, and real-time detection capability are essential characteristics for LET measurement in space radiation, as determined by the nature of the radiation environment. Current detection methodologies can be broadly categorized into active and passive approaches. Passive detection methods, such as solid-

Wenrui Sun and Zhe Cao are with Department of Modern Physics, University of Science and Technology of China, Hefei 230026, China.

Yuxuan Chen is with Institute of Advanced Technology, University of Science and Technology of China, Hefei 230026, China.

Li Wang is with School of Earth and Space Sciences, University of Science and Technology of China, Hefei 230026, China

Yifan Qiao is with School of Emerging Technology, University of Science and Technology of China, Hefei 230026, China, with Hefei National Laboratory, Hefei 230088, China, and also with Department of Modern Physics, University of Science and Technology of China, Hefei 230026, China.

Chunjuan Li, Li Xia, and Yunju Li are with National Key Laboratory for Metrology and Calibration Techniques, China Institute of Atomic Energy, Beijing 102400, China.

(Corresponding author: Zhe Cao, e-mail: caozhe@ustc.edu.cn).

state nuclear track detectors [8] and nuclear emulsions [9, 10], have been widely adopted. These detectors are inexpensive, compact, and feature a low detection threshold. However, their results must be analyzed on the ground, and thus they lack real-time monitoring capability. In contrast, active detectors enable real-time radiation monitoring. Tissue-equivalent proportional counters have been widely used [11, 12], but their uncertainty remains unacceptably high. Recent studies [13] have employed silicon detectors, such as silicon strip detectors [14] and pixel detectors [15], which offer high precision, real-time detection, and a large dynamic range. Among these, double-sided silicon strip detectors (DSSDs) provide broad dynamic range and good position resolution. Using position sensitive detectors, such as DSSDs, to form a silicon telescope can accurately reconstruct particle tracks and measure LET accurately. However, current studies [13-15] exhibit relatively high uncertainty in the low-LET region. In [14], the track measurement uncertainty is about 4%, which can be estimated by the pitch of the detector. In low-LET region, the track resolution is about 11%, mainly because the noise of the electronics affects hit position readout for low energy deposition events.

In this paper, a prototype readout electronics system designed for a real-time LET spectrometer based on DSSDs is proposed. A novel charge dynamic range extension method is used in the prototype system to achieve a large dynamic range and high measurement precision in real-time detection. This paper is organized as follows: section II describes the considerations in the prototype system design, section III describes the hardware design of the prototype readout electronics system, section IV introduces the algorithm implemented in the FPGAs, section V presents the results of the performance tests and joint tests, and finally, section VI concludes this paper.

II. Analysis of System Design Requirements

As discussed in section I, the LET detection requirements can be concluded into two factors: large energy dynamic range to detect particles of $1 \leqslant Z \leqslant 26$; precise track measurement uncertainty of less than 4%. Both the design of the detector and the readout electronics system should be considered.

A. Detector considerations

A silicon telescope based on multi-layer DSSDs is selected as the detector for this study because of its excellent performance. As shown in Fig. 2, (a) is a penetrating particle event, (b) is a stopping particle event. The silicon telescope requires at least three detector layers to distinguish between penetrating and stopping particles based on the response of DSSD3. Furthermore, the symmetrical design enables the telescope to measure particles incident from both the top and bottom directions. The structure of the 3-layer detector is as Fig. 2 shows.

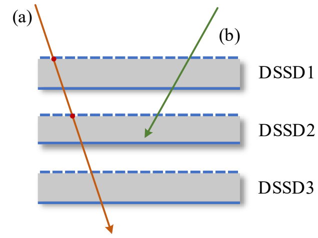

Fig. 2. Structure of detector.

To achieve precise measurement of LET, both accurate track reconstruction and energy measurement are required. The accuracy of track reconstruction is strongly dependent on the detector geometry, which is primarily determined by the interlayer spacing, the scattering of particles in silicon, the strip pitch of the DSSDs, and the transport of electron–hole pairs generated by ionization.

To enhance directional detection capability, the interlayer spacing should be minimized. However, thick silicon can achieve better energy resolution because it deposits more energy. Considering these two factors and structural constraints, an interlayer spacing of 5 mm and silicon thickness of 500 μm could be reasonable choices.

The scattering degree of particles with different atomic numbers and energies in silicon also varies, which has an impact on track measurement. For particles with energy within the range of 0 to 1 GeV/amu, the scattering of protons is the most severe. Scattering of high energy particles is small. The track uncertainty Geant4 [16] simulation results using protons are shown in Fig. 3. Pitch of less than 1600 μm can achieve uncertainty of better than 4%. Protons with energy of less than 13 MeV/amu stop in the second layer of DSSD and are not need to be considered.

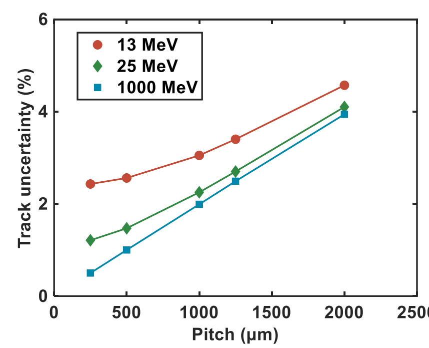

Fig. 3. Simulated relationship between pitch and uncertainty of track.

A narrow strip width can bring good positional resolution, but it will increase the number of readout channels [17]. Considering these two factors, pitch of 1250 μm could be a good choice.

The position readout algorithm also affects the system's position resolution and design complexity. The simulation results based on pitch of 1250 μm and a spacing of 5 mm are shown in Fig. 4. The events within the valid solid angle are mostly readout by a single electrode. Using the maximum signal strip for readout can reduce complexity and almost not lose accuracy.

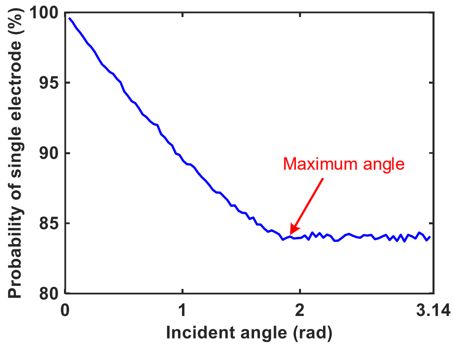

Fig. 4. Simulated relationship between incident angle and probability of single electrode.

B. Charge dynamic range and noise analysis

The relative charge dynamic range can be considered at least 680. The absolute charge dynamic range is determined by the thickness of the silicon d = 500 μm. As the average ionizing energy W in silicon is 3.62 eV, the charge generated by MIPs (0.387 keV/μm in silicon) can be calculated by (2). Considering the situation that all charge collected by single strip, the absolute charge dynamic range is 8.5 fC to 5746 fC.

$$Q = e^{-} * N = e^{-} * \frac{dE/dx \cdot d}{W} \tag{2}$$

The requirement of electronics' noise and trigger threshold are determined by the detection objectives. Geant4 simulations are carried out to determine these requirements. MIPs are selected as target particles, because the signal-to-noise ratio (SNR) is lowest for MIP-induced events. Fig. 5 shows the simulated spectrum of energy deposited by relativistic particles in silicon, which follows a Landau distribution.

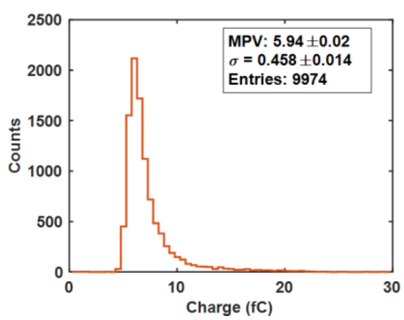

Fig. 5. Deposit energy spectrum of MIPs in 500 μm silicon

The dynamic range of the electronics is also determined by the noise. The noise of the readout electronics is convolved with the energy spectrum to obtain the actual readout energy spectrum. As shown in Fig. 6, the energy spectrum obtained with a noise level of 1 fC broadens the original spectrum. The noise should be less than 1 fC. The trigger threshold is typically set to three times the noise level. Consequently, the relative dynamic range of the electronics should be greater than 5746 times.

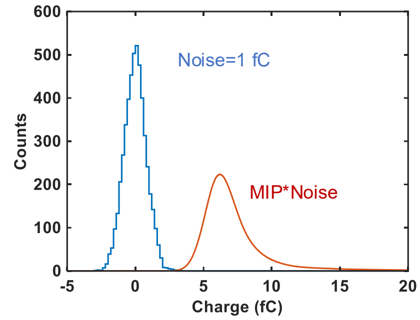

Fig. 6. Energy spectrum of MIPs in 500 μm silicon with noise of 1 fC.

Large dynamic range with high integration and dozens of channels are needed in this spectrometer. The commonly used method to increase the dynamic range is to use additional external channels to achieve multi-gain readout, which significantly reduces integration. This will limit the application scenarios of the spectrometer.

C. Integrated nonlinearity

To resolve the energy peaks of different particles, the energy resolution should be better than 7.5% at 122 MeV, as shown in Fig. 7. The contribution of nonlinearity from the electronics should be less than 2.5%, so that the integral nonlinearity remains below 4.2%, as shown in Fig. 8.

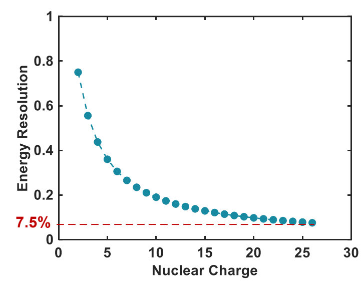

Fig. 7. Energy resolution to distribution adjacent energy peaks of nuclear charge from 1 to 26.

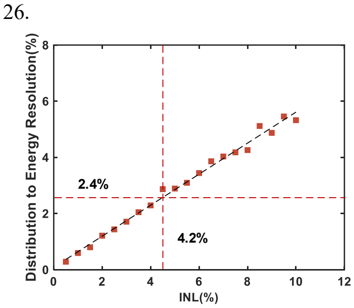

Fig. 8. Relationship between INL and energy resolution.

III. Hardware Design

A. System architecture

As mentioned in section II, a multi-layer structure is selected for the readout electronics system. The electronics are divided into two parts: the front-end and the back-end. The function of the front-end part is to readout charge signals from the DSSDs. This part is designed in layers, each layer corresponding to one detector layer. The back-end part collects data from the front-end part, performs calculations, and helps reduce the overall system size.

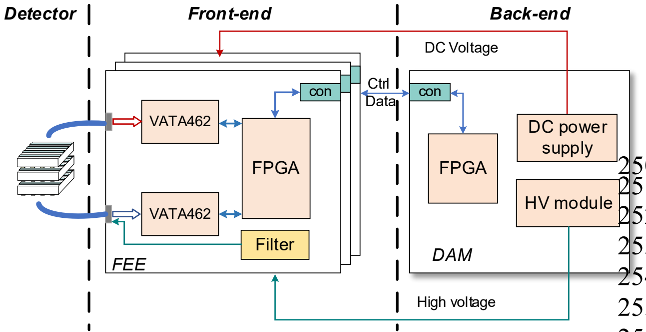

Fig. 9. Architecture of the detectors and the prototype readout electronics

The architecture of the detectors and the prototype readout electronics system is shown in Fig. 9. The prototype system comprises three front-end electronics (FEE) modules and one data acquisition module (DAM). Each FEE is connected to a single-layer DSSD, thereby forming the corresponding front-end section for that layer. The back-end part is integrated into a single DAM, which aggregates and processes data from all FEEs. The DAM also supplies high-voltage (HV) power to the FEEs; this power is filtered before being delivered to the detector. Fig. 10 shows the prototype readout electronics system.

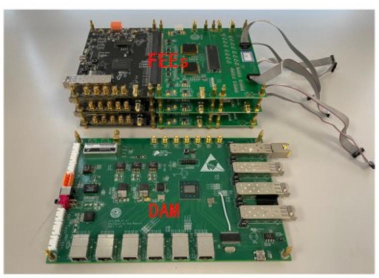

Fig. 10. The prototype readout electronics

B. Design of FEE

As shown in Fig. 11, when a particle traverses a DSSD, it deposits energy in the silicon, generating electron–hole pairs. These pairs are then collected by the electrodes on both sides of the detector. For a single event, the amount of charge collected on the two sides is consistent.

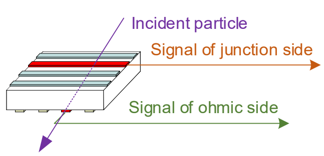

Fig. 11. Readout method for a single layer DSSD.

By simultaneously reading out signals from both sides of the DSSD using high-gain and low-gain channels, the high-gain channel provides higher measurement precision for small signals, while the low-gain channel ensures a wide dynamic range for the electronics. This approach extends the overall dynamic range of the system without compromising precision or increasing the number of channels.

Readout circuits based on charge sensitive amplifiers (CSA) are preferred in space detection, because the data are few and power consumption is low [18-22].

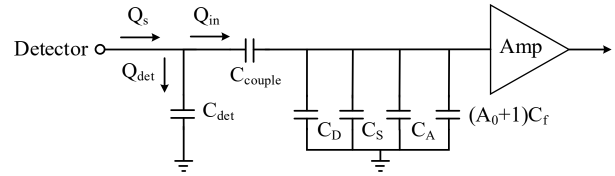

Fig. 12. Model of readout circuit based on CSA.

The gains are set by AC couple capacitors in this work, not by feedback capacitors. As is shown in Fig. 12, the charge Q_s from DSSDs are divided to two paths. Q_i is the charge input to the amplifier, while Q_{det} is the charge loss due to the capacitor of the detector C_{det}. The charge collection efficient ε of the amplifier path can be defined as (3). C_{in} is the total capacitor of the input side of the amplifier, C_{couple} is the AC couple capacitor.

$$\varepsilon = \frac{Q_{in}}{Q_s} = \frac{Q_{in}}{Q_{in}+Q_{det}} = \frac{\frac{C_{in}\cdot C_{couple}}{C_{in}+C_{couple}}}{C_{det}+\frac{C_{in}\cdot C_{couple}}{C_{in}+C_{couple}}} = \frac{1}{1+\frac{C_{det}}{C_{couple}}+\frac{C_{det}}{C_{in}}} \tag{3}$$

The amplifier is configured as a CSA, and C_{in} is usually much larger than C_{det}, the output of the amplifier can be described in (4).

$$V_{out} = K \times \frac{C_{couple}}{C_{couple}+C_{det}} \tag{4}$$

PSpice simulation results are shown in Fig. 13. The results match (4).

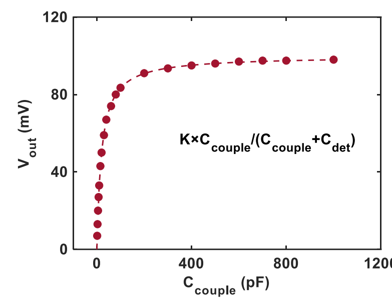

Fig. 13. Simulation results of relationship between C_{couple} and V_{out}

Each FEE module primarily consists of AC coupling capacitors, two application-specific integrated circuits (ASICs) of type VATA462 [23], one field-programmable gate array (FPGA) XC7A100T, one small form-factor pluggable (SFP) module, and power modules. The charge measurement function is mainly performed by the ASICs, which significantly reduces the space required for the electronics, facilitating future space applications.

The ASIC integrates CSAs, shapers, and Wilkinson analog-to-digital converters (ADCs). It provides 32 CSA channels per chip, with a charge dynamic range from -500 fC to 750 fC and a noise level of only 400 e^-, resulting in a relative dynamic range exceeding 7000. However, the overall dynamic range is reduced due to additional noise contributions from the on-chip ADCs. The shapers are divided into two types: a slow shaper for charge measurement and a fast shaper for trigger generation. The 10-bit ADCs digitize the outputs of the slow shapers with tunable charge resolution. Another important factor is the anti-radiation ability. The ASICs' 0.35 µm complementary metal-oxide-semiconductor technique assures its anti-radiation ability [24]. The ASICs are powered by low-noise low dropout regulators (LDOs) to minimize the impact of power rail instability.

Among various ADC architectures, Wilkinson ADCs offer the advantages of high precision and a high level of integration. A slow ramp voltage can achieve high precision. However, for a given number of ADC bits, the achievable precision is constrained by the full-scale dynamic range. This range can be extended by employing FPGA counters to count additional bits, provided that the ADCs generate an over-range output. This approach is illustrated in Fig. 14 and is adopted to further extend the dynamic range of the prototype system.

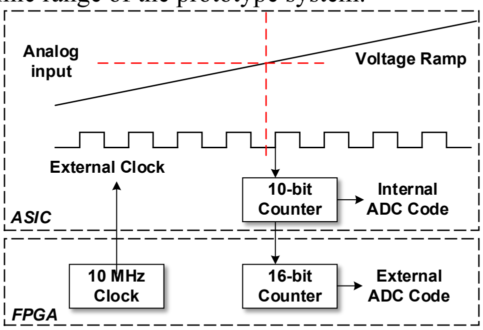

Fig. 14. Diagram of ADCs' dynamic range extension method.

The voltage levels of the ASIC communication ports are incompatible with the standard ports of the FPGA. Fast comparators are employed to shift the voltage levels. The data are sent to the DAM via the SFP module.

C. Design of DAM

The DAM primarily consists of one FPGA XC7K325T, three SFP modules, one Ethernet SFP module, one high-voltage (HV) module, and power modules. It collects data from all FEEs and processes them. DC power is supplied by DC-DC converters on the DAM and is further stepped down to lower voltages by LDOs on each FEE and the DAM, thereby achieving both high efficiency and low noise. The stability of the HV bias directly influences the noise performance of the detector. The Ap002255p05 module produced by iseg is selected as the HV module, as it can provide an HV output of up to 200 V with sufficient current and low noise. Coaxial cables are used to transmit the HV power, and low-pass filters are placed on both the DAM and the FEEs. The HV voltage and current are monitored by precision ADCs on the DAM to detect any faults in the HV supply or the detectors. The HV voltage is controlled by the DAM FPGA in conjunction with a DAC.

IV. Firmware of the FPGAs Design

Both FEEs and DAM use FPGAs as controllers and data processors. FPGAs in FEEs execute slow control of ASICs and communicate with DAM FPGA. FPGA in DAM processes data and trigger coincidence. The design of FPGAs are as follows.

A. Design of FEE FPGA firmware

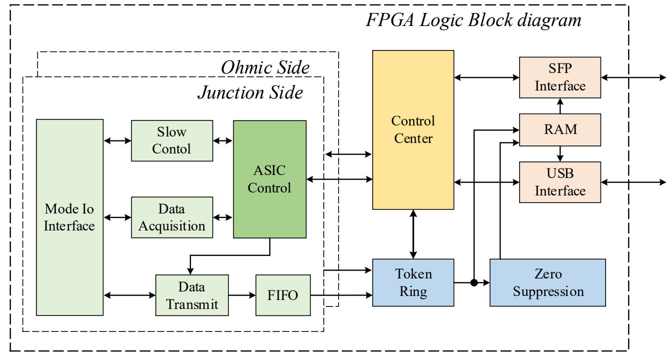

Fig. 15. Block diagram of the FEE FPGA logic.

FPGAs in FEEs mainly have four functions: slow control of ASICs, data readout from ASICs, data package, and data upload to DAM FPGA. The block diagram of the FEE FPGA logic is shown in Fig. 15. Configuration registers of the ASICs are configured through slow control module before working in data readout mode. These registers are different for two ASICs because the input signals' polarity is different. The data from both ASICs on single FEE are readout by token ring structure. The data can be suppressed to reduce data volume.

B. Design of DAM FPGA firmware

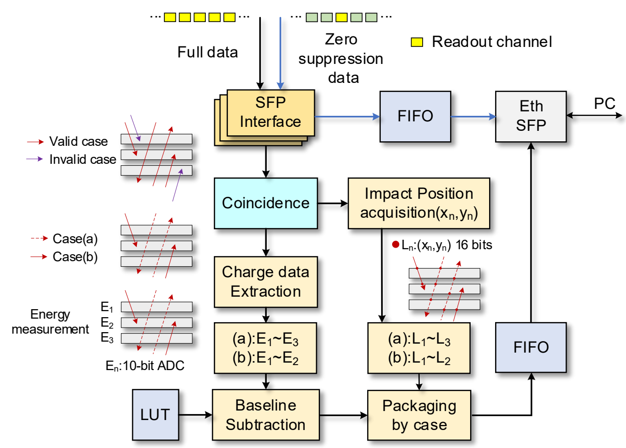

Fig. 16. Block diagram of the DAM FPGA logic.

Fig. 16 shows the block diagram of the DAM FPGA logic. A coincidence and information extraction logic module within the FPGA processes the data and uploads them to the PC via an Ethernet SFP module. Events are classified into three categories: invalid events, valid events with two layers triggered, and valid events with three layers triggered. If the interval between consecutive events exceeds the trigger window, they are considered invalid. Events involving only non-adjacent layers are also deemed invalid, even if they occur within the same trigger window. Events with two adjacent triggered layers or all three triggered layers are both considered valid, but they employ different LET calculation methods. Cases with two layers triggered arise from stopped particles; Equations (5) [25] and (6) present the approach for calculating the incident depth within the middle layer.

$$R_{Al} = \begin{cases} 14.21E_p^{1.5874} & 1\ MeV < E_p < 2.7\ MeV \\ \dfrac{10.5E_p^2}{0.68+0.434\,ln(E_p)} & 2.7\ MeV < E_p < 20\ MeV \end{cases} \tag{5}$$

$$\frac{R_1}{R_2} = \frac{\rho_1}{\rho_2}\sqrt{\frac{M_1}{M_2}} \quad (6)$$

For events with three layers triggered, the depth of the other layers can be directly calculated from the detector thickness and the incident angle, which can be determined from the hit position on the detectors. The hit position corresponds to the location of the triggered strips, since in most cases, almost all charge is collected by a single strip. Minimal improvement can be obtained through additional processing, and the same applies to energy calculation. The deposited energy in each layer is correlated with the charge collected by the triggered strip, which will be calibrated using a standard radiation source. The electronic baseline will be subtracted prior to calculation. The total deposited energy is the sum of the energies from all triggered layers. The LET value can then be calculated using equation (1).

V. TEST RESULTS

A. *Electronics tests*

The dynamic range and equivalent noise charge (ENC) of the prototype system were evaluated. The dynamic range was measured using an arbitrary waveform generator (AWG) AFG3252 and passive attenuators. The AWG generated pulse signals with varying amplitudes, which were then fed into the FEEs through the attenuators and converted into charge signals via 1 pF capacitors. A block diagram of the electronic test setup is shown in Fig. 17.

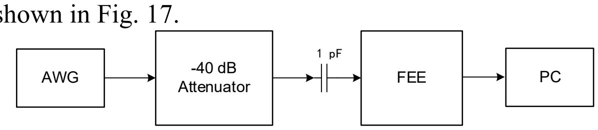

Fig. 17. Block diagram of the electronics tests.

The ASICs have multiple gains to select. Maximum and minimum gain settings were tested. Dynamic range extension method was not used in this test and was tested along. The results are shown in Fig. 18. The maximum-gain channels exhibit a dynamic range of approximately 80 fC, while the minimum-gain channels provide a dynamic range of about 700 fC. Charge of 700 fC is the maximum dynamic range of the ASIC, so that in the maximum-gain channels the dynamic range can be extended to 700 fC by using the extension method. The ENC of all readout channels in the high-gain mode of the prototype is presented in Fig. 19. The ENC was measured with the electronics inputs left floating. For most channels, the ENC is less than 0.11 fC, yielding a dynamic range of approximately 6000.

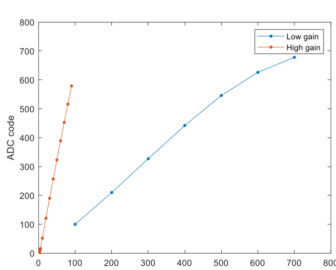

Fig. 18. Tested dynamic range of one layer FEE.

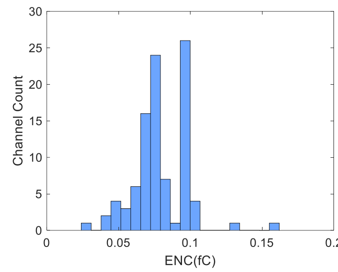

Fig. 19. ENC of all 96 channels in maximum-gain configuration.

The dynamic range and INL are tested with ADCs' dynamic range extension method. As is shown in Fig. 20, the INL is 3.23% in charge dynamic range of less than 700 fC.

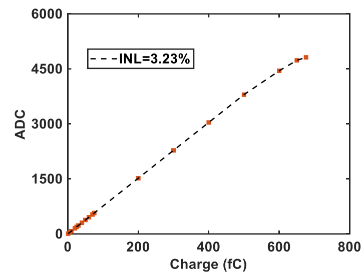

Fig. 20. Test results of charge dynamic range and INL with ADCs' dynamic range extension method.

B. *Calibration tests*

To calibrate the readout electronics system, calibration tests were carried out using DSSDs. A mixed standard alpha radiation source was used in energy calibration, all energy of the alpha radiation will deposit in one-layer DSSD. The parameters of the source are shown in table I. The block diagram of calibration tests is shown in Fig. 21. The prototype was calibrated layer by layer. The mixed source was placed very close to the detector, and is collimated by polymethyl methacrylate board with circle holes.

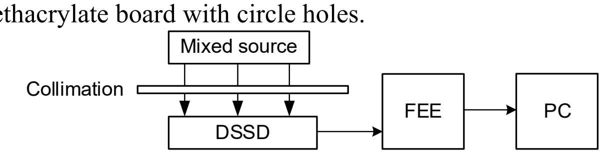

Fig. 21. Block diagram of the calibration tests.

TABLE I
PARAMETER OF THE MIXED RADIATION SOURCE

^{241}Am			^{239}PU			^{244}Cm		
Energy /MeV	Ratio	Average energy /MeV	Energy /MeV	Ratio	Average energy /MeV	Energy /MeV	Ratio	Average energy /MeV
5.48	0.85	5.45	5.11	0.12	5.15	5.76	0.24	5.79
5.44	0.13		5.14	0.15				
5.38	0.02		5.16	0.73		5.80	0.76	
5.54	0.00							

To precisely calibrate the prototype, a simulation using MCNPX was carried out. The model includes radiation source, the polymethyl methacrylate board and the detector. Simulated deposit energy is 5.02 MeV for ^{239}Pu, 4.65 MeV for ^{241}Am, and 4.32 MeV for ^{244}Cm. The test results are shown in Fig. 22. Both sides have three distinguish peaks related to three materials of the source. The resolution is better than 2.41%@4.65 MeV for both sides of the detector.

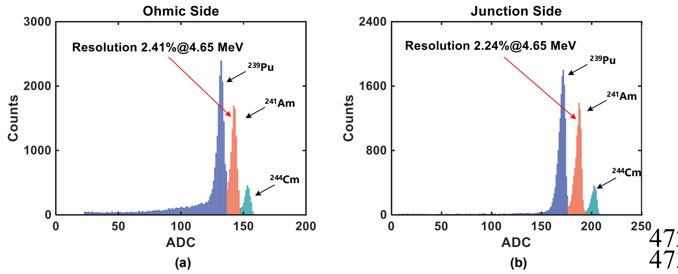

Fig. 22. Typical results for energy calibration using mixed radiation source. (a) Calibration results of DSSD's ohmic side. (b) Calibration results of DSSD's junction side.

The charge distribution method was tested using a standard ^{241}Am source. The deposit energy is almost the same for each event, so that the detector generates the same quantity of charge. The test results are shown in Fig. 23. It shows the same relation as the simulation results in section II.

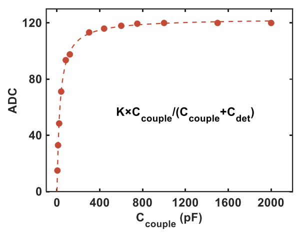

Fig. 23. Test results of charge distribution method. The solid dots are the test results, and the short dashes are the fitted results.

C. Neutron field tests

To evaluate the LET measurement capability, a neutron radiation field test was conducted. Fig. 24 shows the on-site test setup. A three-layer silicon telescope, consisting of three DSSDs, was used as the detector. Each DSSD had 16 strips on both sides, with the strips on opposite sides oriented perpendicular to each other. The detectors and the prototype system were housed in an aluminum box. The box was placed in a neutron irradiation field, approximately 1 meter from the neutron source. A 1 mm thick polyethylene layer was used to convert neutrons into protons, which then struck the DSSDs. The primary neutron energy was approximately 14.8 MeV.

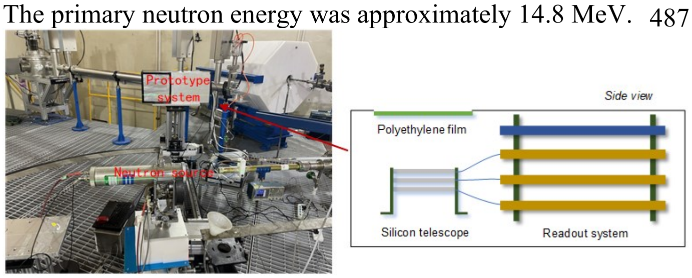

Fig. 24. On-site test configuration.

To validate the on-site test results, a Geant4 simulation was performed. The simulation model is illustrated in Fig. 25. It consists of a 14.8 MeV point neutron source, a 1-mm-thick polyethylene film, and the detector. The distance between the point source and the center of the polyethylene film is 1 m. The area of the polyethylene film is significantly larger than that of the DSSDs. Due to the scattering effect within the conversion medium, the incident angle of protons striking the DSSDs may deviate from the line connecting the hit point and the point source. Fig. 26 shows the total deposited energy obtained from the simulation. The corresponding calculated LET values are presented in Fig. 29.

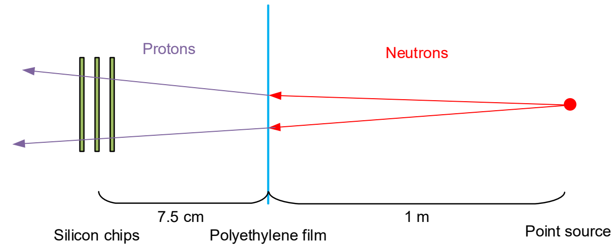

Fig. 25. Model of Geant4 simulation.

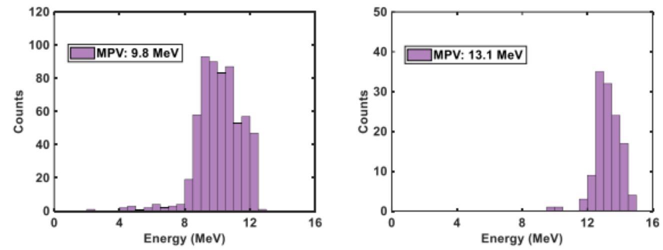

Fig. 26. Total deposit energy in simulation results.

The measured total deposited energy results are shown in Fig. 27. The most probable value (MPV) of the total deposited energy for stopped particles is 10.6 MeV experimentally, while the simulated MPV is 9.8 MeV. For particles traversing all three layers of DSSDs, the experimental MPV is 13.6 MeV, compared to the simulated value of 13.1 MeV. The experimental results are in good agreement with the simulation results presented in Fig. 26.

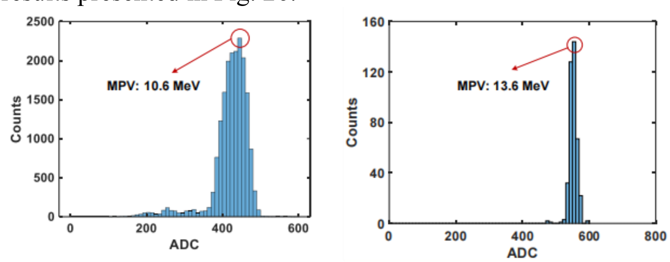

Fig. 27. Total deposit energy in test results.

Fig. 28 shows two trace reconstruction results. The traces are successfully reconstructed for both cases with 2 layers triggered and with 3 layers triggered.

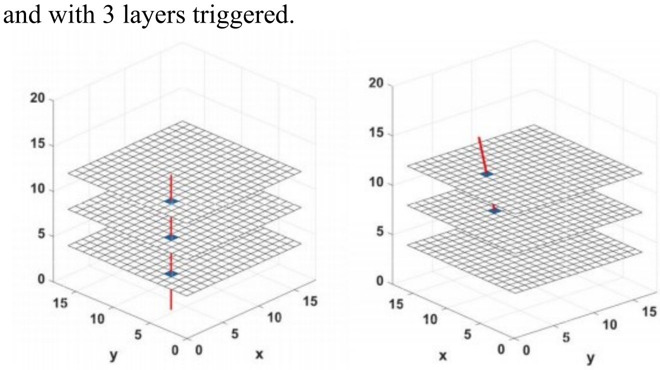

Fig. 28. Typical track reconstruction results of through particles and stopped particles.

The calculated LET spectrum of stopped events is shown in Fig. 29. The tested MPV is 19 keV/μm, which is very close to the simulated MPV of 18 keV/μm. The test results show the prototype works well.

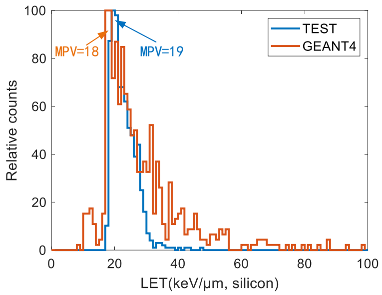

Fig. 29. Calculated LET spectrum.

VI. Conclusion

A prototype readout electronics system for LET spectrometer was designed for space radiation detection. Precise LET spectrums can be obtained from accurate measurement of hit position and energy loss of incident particle in real-time. The energy dynamic range is extended to about 6000 times by readout opposite sides of the DSSDs using different gains and ADC dynamic range extension method. The calibration tests show that the prototype has excellent energy resolution. The neutron radiation field test results meet the Geant4 simulation results.

Acknowledgment

This work was supported in part by the National Natural Science Foundation of China (Grant No. 11875252).

References

[1] J. L. Barth, C. S. Dyer and E. G. Stassinopoulos, “Space, atmospheric, and terrestrial radiation environments,” in IEEE Trans. Nucl. Sci., vol. 50, no. 3, pp. 466-482, Jun. 2003, 10.1109/TNS.2003.813131.
[2] J. D. Wrbanek, S. Y. Wrbanek, “Space radiation and impact on instrumentation technologies,” NASA, 2020.
[3] ICRU, “Linear energy transfer,” ICRU Report 16, 1970.
[4] I. Jun, et al., “A review on radiation environment pathways to impacts: Radiation effects, relevant empirical environment models, and future needs,” Adv. Space Res., Apr. 2024, 10.1016/j.asr.2024.03.079.
[5] William R. Leo, “Techniques for Nuclear and Particle Physics Experiments,” 1994.
[6] G. Dietze, et al., “ICRP Publication 123: Assessment of radiation exposure of astronauts in space,” Ann. ICRP, vol. 42, no.5, pp. 1-339, 2013, 10.1016/j.icrp.2013.05.004.
[7] M. M. Shapiro, “Composition and Origin of Cosmic Rays,” NATO ASI Series C, 1983.
[8] A. B. Akopova, M. M. Manaseryan, A. A. Melkonyan, S. Sh. Tatikyan, Yu. Potapov, “Radiation measurement on the International Space Station,” Rad. Meas., vol. 39, no.2, pp. 225-228, 2005, 10.1016/j.radmeas.2004.06.013.
[9] T. Doke, et al., “Real time measurement of LET distribution in the IML-2 Space-Lab (STS-65),” Nucl. Instrum. Methods Phys. Res. A, vol. 365, no. 2-3, pp.524-532, 1995, 10.1016/0168-9002(95)00523-4.
[10] M.A. Rana, “CR-39 nuclear track detector: An experimental guide,” Nucl. Instrum. Methods Phys. Res. A, vol. 910, pp. 121-126, 2018, 10.1016/j.nima.2018.08.077.
[11] V.D. Nguyen, et al., “Real time quality factor and dose equivalent meter “CIRCE” and its use on-board the Soviet orbital station “MIR”,” Acta Astronautica, vol. 23, pp. 217-226, 1991, 10.1016/0094-5765(91)90121-K.
[12] N. M. Hayes, et al., “Active Tissue Equivalent Dosimeter: A Tissue Equivalent Proportional Counter flown onboard the International Space Station,” Nucl. Instrum. Methods Phys. Res. A, vol. 1028, 2022, 10.1016/j.nima.2022.166389.
[13] T. Doke, et al., “Application of real-time radiation dosimetry using a new silicon LET sensor,” Mutat. Res., vol. 430, no. 2, pp. 191-202, Dec. 1999, 10.1016/s0027-5107(99)00130-x.
[14] J. Labrenz, et al., “Matroshka DOSTEL measurements onboard the International Space Station (ISS),” JSWSC, vol. 5, 2015, 10.1051/swsc/2015039.
[15] M. Kroupa, et al., “A semiconductor radiation imaging pixel detector for space radiation dosimetry,” Life Sci. Space Res., vol. 6, pp. 69-78, 2015, 10.1016/j.lssr.2015.06.006.
[16] S. Agostinelli, et al., “Geant4 – a simulation toolkit,” Nucl. Instrum. Meth. A, vol 506, no. 3, pp.250-303, 2003, 10.1016/S0168-9002(03)01368-8.
[17] G. Ambrosi, et al., “The spatial resolution of the silicon tracker of the Alpha Magnetic Spectrometer,” Nucl. Instrum. Methods Phys. Res. A, vol. 869, pp. 29-37, 2017, 10.1016/j.nima.2017.07.014.
[18] C. Feng, “The research on the readout electronics for the calorimeter detector of the dark matter exploration satellite,” Ph.D. dissertation, Dept. Phys., Univ. of Sci. and Tech. of China, Hefei, Anhui, 2011. p. 33.
[19] S. Ting, “The Alpha Magnetic Spectrometer on the International Space Station,” Nucl. Phys. B - Proceedings Supp., vol. 243-244, pp. 12-24, 2013, 10.1016/j.nuclphysbps.2013.09.028.
[20] P. Azzarello, et al., “The DAMPE silicon–tungsten tracker,” Nucl. Instrum. Methods Phys. Res. A, vol. 831, pp. 378-384, 2016, 10.1016/j.nima.2016.02.077.
[21] L. Wang, et al., “Prototype readout electronics of a double-sided silicon strip detector for space exploration,” Rev. Sci. Instrum., vol. 92, no. 11, 2021, 10.1063/5.0067083.
[22] G. Chen, et al., “Low-Power Large-Dynamic Range Readout ASIC for VLAST Silicon Strip Detectors,” *IEEE Trans. Nucl. Sci.*, vol. 72, no. 3, pp. 567-574, March 2025, 10.1109/TNS.2024.3451952.
[23] Integrated Detector Electronics AS[Online]. http://www.ideas.no
[24] J. Kaplon, “Front-end electronics for silicon strip trackers: Architectures and evolution,” Nucl. Instrum. Methods Phys. Res. A, vol. 1045, Jan. 2023, 10.1016/j.nima.2022.167570.
[25] N. Tsoulfanidis, L. Sheldon, “Measurement and Detection of Radiation (5th ed.),” CRC Press, 2021, 10.1201/9781003009849.